

See discussions, stats, and author profiles for this publication at: <https://www.researchgate.net/publication/231644952>

# Cobalt Oxide Nanomaterials by Vapor-Phase Synthesis for Fast and Reversible Lithium Storage

ARTICLE *in* THE JOURNAL OF PHYSICAL CHEMISTRY C · MAY 2010

Impact Factor: 4.77 · DOI: 10.1021/jp102380e

---

CITATIONS

39

READS

41

## 9 AUTHORS, INCLUDING:



[Davide Barreca](#)

National Research Council, Padova

289 PUBLICATIONS 4,316 CITATIONS

[SEE PROFILE](#)



[Alberto Gasparotto](#)

University of Padova

255 PUBLICATIONS 2,968 CITATIONS

[SEE PROFILE](#)



[Cinzia Sada](#)

University of Padova

219 PUBLICATIONS 3,225 CITATIONS

[SEE PROFILE](#)



[Luis Sánchez](#)

University of Cordoba (Spain)

93 PUBLICATIONS 1,648 CITATIONS

[SEE PROFILE](#)

# Cobalt Oxide Nanomaterials by Vapor-Phase Synthesis for Fast and Reversible Lithium Storage

D. Barreca,\*† M. Cruz-Yusta,‡ A. Gasparotto,§ C. Maccato,§ J. Morales,‡ A. Pozza,§ C. Sada,||  
L. Sánchez,\*‡ and E. Tondello§

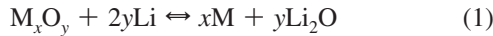
CNR-ISTM and INSTM, Department of Chemistry, Padova University, 35131 Padova, Italy, Departamento de Química Inorgánica e Ingeniería Química, Universidad de Córdoba, 14071 Córdoba, Spain, Department of Chemistry, Padova University and INSTM, 35131 Padova, Italy, and Department of Physics and CNISM, Padova University, 35131 Padova, Italy

Received: March 16, 2010; Revised Manuscript Received: April 26, 2010

The design and assembly of suitable nanosystems are key issues in the development of smaller and more efficient lithium batteries. To this regard, cobalt oxides possess very favorable properties for use as negative electrode materials. In this work, we describe a convenient synthesis route to cobalt oxide nanomaterials (both single- and mixed-phase CoO and  $\text{Co}_3\text{O}_4$ ) supported on Ti. The systems are grown by chemical vapor deposition starting from an innovative second-generation molecular source,  $\text{Co}(\text{hfa})_2 \cdot \text{TMEDA}$  ( $\text{hfa} = 1,1,1,5,5,5$ -hexafluoro-2,4-pentanedionate, TMEDA =  $N,N,N',N'$ -tetramethylmethylenediamine). Controlled variations of the substrate temperature and  $\text{O}_2$  pressure in the reaction atmosphere enabled tailoring both the phase composition and the system morphology. The electrochemical properties of the obtained nanosystems were evaluated by galvanostatic measurements and impedance spectroscopy. The results showed excellent cycling performances and very high specific capacity values, offering attractive perspectives for the use of the present systems as advanced anode materials in Li-ion batteries.

## Introduction

Rechargeable lithium-ion batteries are extremely promising power sources for portable electronic devices in a variety of consumer and medical products, owing to their high energy density, lightweight, long service life, and absence of memory effects.<sup>1–5</sup> In the last decades, the ever-increasing request for high capacity/power has fueled intensive efforts devoted at improving cell performances through the development of electrodes with a good rate capability and an enhanced cycle life.<sup>6</sup> To this regard, there has been growing evidence that nanostructured materials provide improved electrochemical performances with respect to their bulk counterparts thanks to their short path length for  $\text{Li}^+$  transport and high surface area, favoring an efficient electrode–electrolyte contact.<sup>2,6,7</sup> In particular, oxides of 3d transition metals have emerged as alternative anode materials with very attractive electrochemical performances, ascribed to the reaction<sup>8–11</sup>



The  $\text{Li}_2\text{O}$  formed in the reduction process behaves as an electrochemically active material in the reverse reaction, catalyzed by the presence of metal nanoparticles.<sup>8</sup> Among transition-metal oxide nanostructures, cobalt oxides ( $\text{Co}_x\text{O}_y$ , namely, CoO and  $\text{Co}_3\text{O}_4$ ) have received considerable attention

and several studies have been focused on their preparation in various forms (e.g., nanocubes, nanowires, nanowalls, nanotubes, thin films...) in order to tailor their electrochemical performances.<sup>12–18</sup> Among the adopted synthesis processes, it is worth mentioning wet chemical routes,<sup>9,12,14,17–19</sup> solid-state syntheses,<sup>20</sup> hydrothermal or microwave methods,<sup>21–25</sup> and template-assisted strategies involving porous membranes, carbon nanotubes, or viruses.<sup>5,17,26–28</sup> In addition, supported cobalt oxide electrodes based on thin films and 1D systems have been obtained by electrodeposition,<sup>13</sup> pulsed laser deposition,<sup>15,29</sup> and liquid-phase processes.<sup>30</sup> Nevertheless, the development of  $\text{Co}_x\text{O}_y$  anodes for practical use is still largely hindered by the modest capacity retention, which still falls short of meeting technological demands.<sup>19,20</sup> In fact, only a few reports devoted to cobalt oxide nanoelectrodes retaining a high storage capacity at elevated test currents are available up to date.<sup>22–26,28,30</sup> These observations highlight the strategic need of alternative synthetic approaches to supported  $\text{Co}_x\text{O}_y$  nanomaterials, enabling a precise control on their structure and spatial organization in order to fully exploit their applicative potential.<sup>21,26</sup>

In this paper, we present an innovative route for the preparation of supported cobalt oxide nanoelectrodes. The adopted procedure represents an implementation of the already tested, successful deposition of cobalt oxide nanosystems on Si(100).<sup>31</sup> In particular, the target nanomaterials were grown on Ti using a chemical vapor deposition (CVD) route from a novel precursor,  $\text{Co}(\text{hfa})_2 \cdot \text{TMEDA}$  ( $\text{hfa} = 1,1,1,5,5,5$ -hexafluoro-2,4-pentanedionate, TMEDA =  $N,N,N',N'$ -tetramethylmethylenediamine).<sup>32,33</sup> Besides the inherent experimental flexibility and amenable scalability, a key advantage of the proposed approach is the absence of ancillary materials (e.g., binders, conductors).<sup>10,12,14,17,20–22,27,29,34</sup> In addition, the proposed strategy is an attractive alternative for a careful tailoring of nanomaterial phase composition (CoO vs  $\text{Co}_3\text{O}_4$ ) and morphologi-

\* To whom correspondence should be addressed. Phone: +39-049-8275170 (D.B.), 34-957-218620 (L.S.). Fax: +39-049-8275161 (D.B.), 34-957-218621 (L.S.). E-mail: davide.barreca@unipd.it (D.B.), luis.sanchez@uco.es (L.S.).

† CNR-ISTM and INSTM, Department of Chemistry, Padova University.

‡ Universidad de Córdoba.

§ Department of Chemistry, Padova University and INSTM.

|| Department of Physics and CNISM, Padova University.

**TABLE 1: Growth Conditions Adopted for the CVD of Cobalt Oxide Nanomaterials and Corresponding Phase Composition. The Sample Mean Particle Sizes and the Root Mean Square (rms) Roughness Values Obtained By Atomic Force Microscopy (AFM) Analyses Are Also Reported<sup>a</sup>**

sample	substrate temperature (°C)	total pressure (mbar)	composition	nanodeposit thickness (nm)	particle size (nm)	rms roughness (nm)
<b>A</b>	400	3.0	CoO	67 ± 19	15	122
<b>B</b>	500	3.0	CoO + Co <sub>3</sub> O <sub>4</sub>	245 ± 60	30	149
<b>C</b>	400	10.0	Co <sub>3</sub> O <sub>4</sub>	418 ± 71	150	77
<b>D</b>	500	10.0	Co <sub>3</sub> O <sub>4</sub>	475 ± 80	400	96

<sup>a</sup> The total O<sub>2</sub> flow rates were 40 and 200 sccm for experiments performed at a total pressure of 3.0 and 10.0 mbar, respectively. In all cases, the total deposition duration was 2 h.

cal organization, key issues to achieve improved functional performances in innovative Li-cell anodes.

## Experimental Procedures

**Synthesis.** Prior to each synthesis, Ti substrates (Aldrich, 0.25 mm thick, 99.7%, size = 8 × 8 mm<sup>2</sup>) were ultrasonically degreased in dichloromethane, subsequently rinsed in isopropanol, and finally dried in air. CVD depositions were performed under O<sub>2</sub>-based atmospheres in a tubular cold-wall reactor endowed with a resistively heated susceptor.<sup>35,36</sup> Co(hfa)<sub>2</sub>·TMEDA, synthesized according to the literature,<sup>32</sup> was placed in a vaporization reservoir maintained at 60 °C. The pressure and gas flow rates were measured by a capacitance manometer (BOC Edwards) and mass flow controllers (MKS), respectively. The tubing and valve system were heated to 120 °C to avoid undesired precursor condensation phenomena. Prior to each experiment, a preliminary degassing of the whole CVD system down to ≈10<sup>-2</sup> mbar was performed by means of a rotary pump (BOC Edwards). The optimized experimental parameters used in the present work are reported in Table 1.

**Structural Characterization.** Glancing incidence X-ray diffraction (GIXRD) measurements were carried out at a fixed incidence angle of 1.0° by means of a Bruker D8 Advance diffractometer equipped with a Göbel mirror and a Cu Kα source operated at 40 kV and 40 mA. The average crystallite dimensions were estimated from line broadening by means of the Scherrer equation.

**Chemical Composition.** Secondary-ion mass spectrometry (SIMS) measurements were performed with an IMS 4f mass spectrometer (Cameca) using a 14.5 KeV Cs<sup>+</sup> primary beam and by negative secondary-ion detection. Spectra were collected at a 20 nA primary beam intensity (beam stability better than 0.7%), using an electron gun for charge compensation. A beam blanking mode (i.e., interruption of the sputtering process during magnet stabilization periods) was adopted to improve the in-depth resolution, using a high mass resolution configuration to avoid mass interference artifacts. For each sample, the erosion speed was evaluated at various depths, measuring the corresponding crater by means of a Tencor Alpha Step profiler. The dependence of the sputtering rate on the material composition was, therefore, taken into account in the depth value determination. The lateral specimen homogeneity was checked by performing SIMS analysis in various points.

**Morphological Analysis.** The morphological features of the samples were investigated by a joint field emission-scanning electron microscopy (FE-SEM) and atomic force microscopy (AFM) characterization. FE-SEM measurements were performed by a Zeiss SUPRA 40 VP instrument operated at an acceleration voltage of 10.0 kV. AFM analyses were carried out by using a Nanoscope IIIa AFM (Digital Instruments) operated in contact mode, employing SiN cantilevers (Veeco) with a spring constant

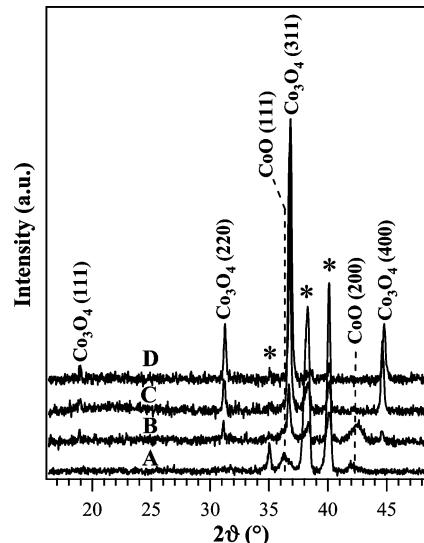


**Figure 1.** GIXRD spectra for cobalt oxide nanosystems. Stars (\*) mark reflections attributed to the Ti substrate.

of 0.73 N·m<sup>-1</sup>. rms roughness values were calculated from the height profile of the images.

**Electrochemical Tests.** Electrochemical measurements were performed in two electrode swagelok-type cells, using lithium as a counter electrode and a Merck battery electrolyte LP 40 (ethylene carbonate (EC)-diethyl carbonate (DEC), EC/DEC = 1:1 w/w, 1 M LiPF<sub>6</sub>). Titanium pieces (8 × 8 mm<sup>2</sup>) coated with the active cobalt oxide nanomaterial were used as working electrodes. The oxide amount on each sample was determined by weighing the Ti substrate before and after deposition on a Sartorius microbalance (sensitivity = ± 1 µg). Cells were galvanostatically charged and discharged at different cycling rates, from 0.05 to 2 C (C was defined as 715, 850, and 890 mA·h·g<sup>-1</sup> for CoO, CoO/Co<sub>3</sub>O<sub>4</sub>, and Co<sub>3</sub>O<sub>4</sub> samples, respectively). The electrochemical measurements were controlled via a MacPile potentiostat–galvanostat. Electrochemical impedance spectroscopy (EIS) analyses in the frequency range of 10<sup>-5</sup> to 90 kHz (amplitude = 3 mV) were performed by means of a Solartron 1470 battery test unit coupled to a Schlumberger SI 1255 response analyzer.

## Results and Discussion

GIXRD patterns of cobalt oxide specimens obtained under different conditions are displayed in Figure 1. Concerning sample A, synthesized at 400 °C and 3.0 mbar total pressure, two broad weak reflections centered at 2θ = 36.4 and 42.1° were detected and attributed to the (111) and (200) peaks of the rocksalt CoO phase.<sup>37</sup> The presence of nanocrystalline structures and/or structural disorder was likely responsible for the large full width at half-maximum (fwhm) of these signals.

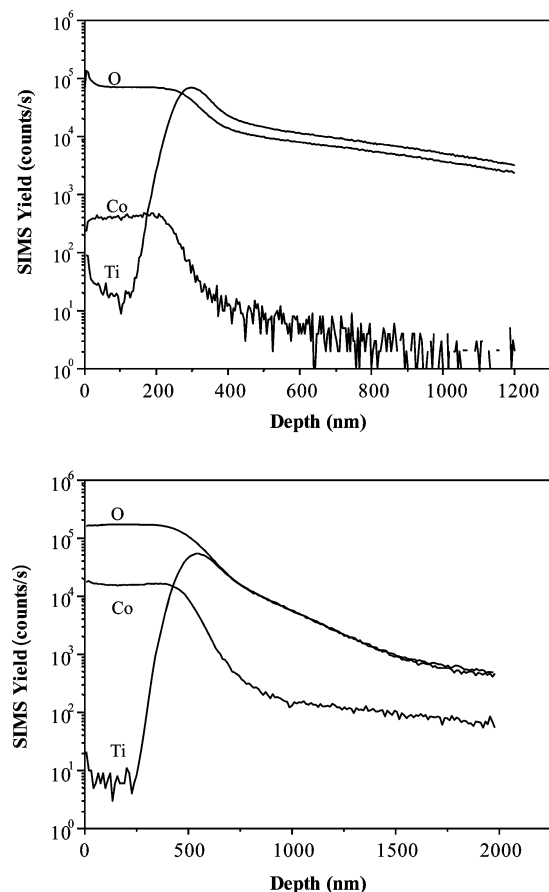


**Figure 2.** Representative SIMS depth profiles for specimens deposited at 500 °C: **B** (upper) and **D** (lower).

An increase in the growth temperature up to 500 °C (sample **B**) resulted in a broadening and upward shift of the CoO peaks, along with the appearance of additional diffraction signals at  $2\vartheta = 18.9, 31.1, 36.7$ , and  $44.6^\circ$ , associated, respectively, with (111), (220), (311), and (400) planes of cubic  $\text{Co}_3\text{O}_4$ .<sup>38</sup> For specimens **C** and **D**, obtained at 10.0 mbar total pressure,  $\text{Co}_3\text{O}_4$  was the only detected crystalline phase and its reflections underwent an appreciable intensity increase with respect to samples **A** and **B**. The present results indicated that the selective obtainment of CoO was possible only under mild oxidative conditions, that is, lower growth temperatures and reduced oxygen content in the reaction atmosphere, in line with previous reports.<sup>31,39</sup> As evaluated from the Scherrer equation, the typical average nanocrystallite size was 15 and 38 nm at 3.0 and 10.0 mbar total pressure, respectively.

Information on the system chemical composition was obtained by SIMS depth profiling. As a general trend, all the examined deposits presented a clearly detectable interface with the Ti substrate. As an example, the in-depth distributions of Co, O, and Ti for specimens obtained at 500 °C are reported in Figure 2. The remarkable similarity in the profiles of cobalt and oxygen ionic yields throughout the nanodeposit thickness suggested a common chemical origin of these species.

The measured thickness values obtained after depth profiling are reported in Table 1. As can be noted, the use of higher deposition temperatures and, in particular, of higher overall oxygen pressures resulted in an appreciable increase of the nanodeposit thickness, indicating thus that the growth process was effectively enhanced by the use of more oxidizing conditions.

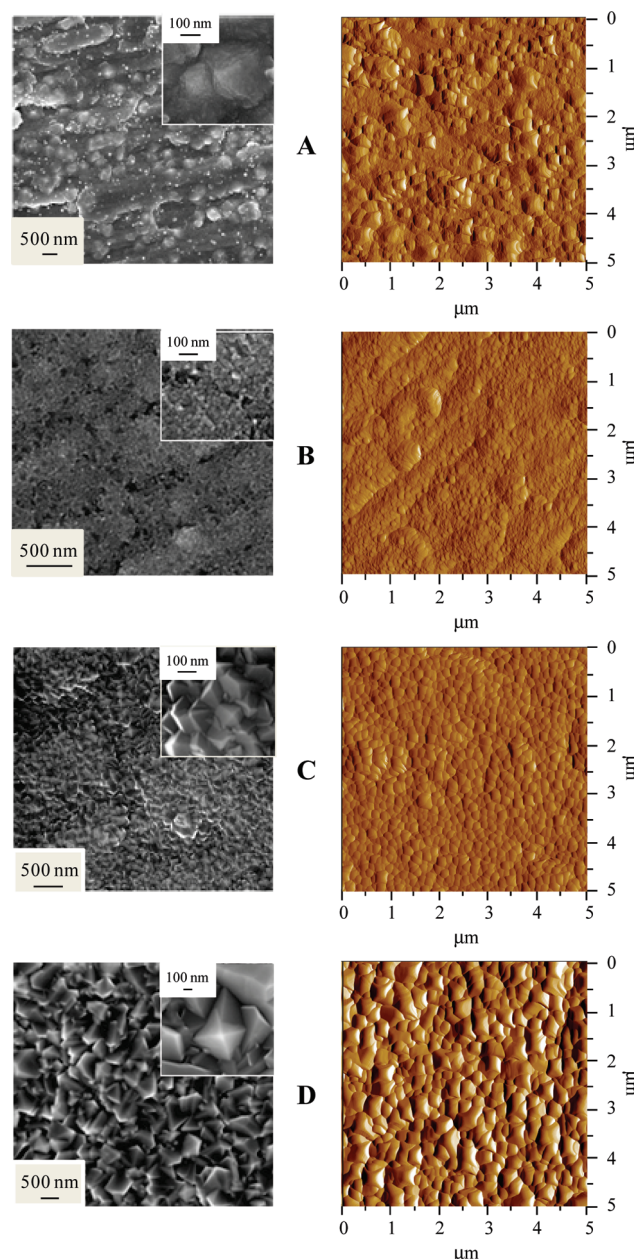


**Figure 3.** Representative plane-view FE-SEM images and AFM micrographs of Ti-supported cobalt oxide nanomaterials.

The nanosystem morphology, investigated by the combined use of FE-SEM and AFM surface analyses (Figure 3), revealed an appreciable dependence on the adopted growth parameters. As can be observed, sample **A** (i.e., the thinnest one) was dominated by a rough texture mainly attributed to the intrinsic corrugation of the titanium substrate. A closer inspection of the recorded micrographs (see the inset) revealed a uniform conformal coverage of the Ti substrate by low-sized CoO nanoparticles (15 nm). A comparison of the latter value with the nanocrystal size computed by GIXRD suggested that the observed grains were mainly single crystallites. In agreement with the already discussed thickness increase, specimen **B** presented a more effective coverage of the underlying Ti substrate, characterized by a homogeneous distribution of 30 nm nanoaggregates well interconnected among themselves. The presence of such particles was typical for a 3D growth mode of the corresponding nanodeposit.

A completely different morphological organization was observed for samples **C** and **D**, obtained at 10.0 mbar total

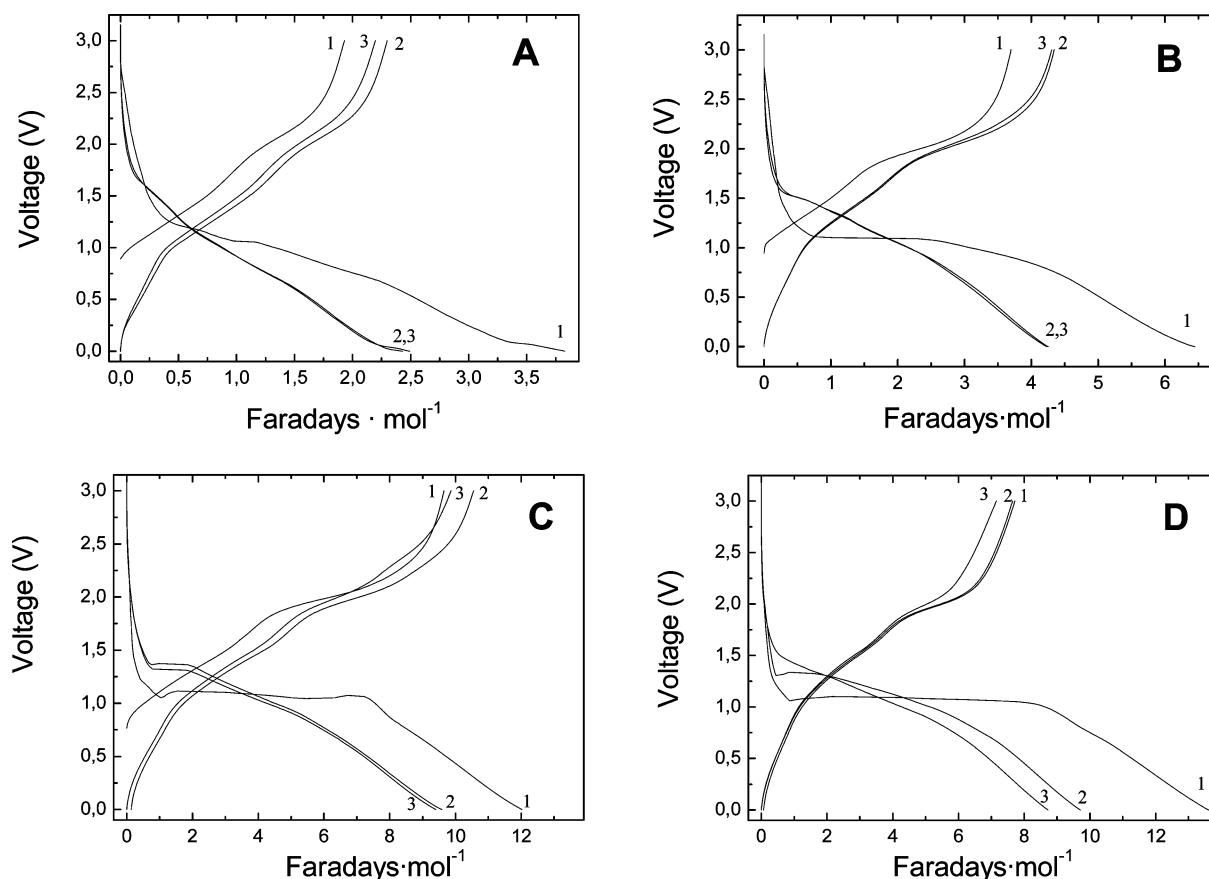


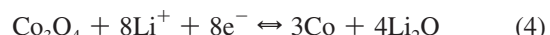
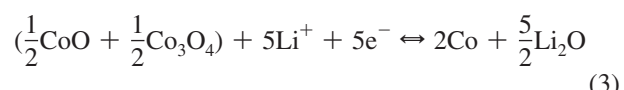
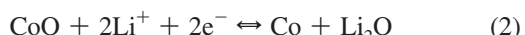
**Figure 4.** Charge/discharge voltage profiles during the first three operational cycles (1, 2, 3) for samples **A–D** cycled between 3.0 and 0.0 V (vs Li/Li<sup>+</sup>).

pressure and characterized by the presence of the sole Co<sub>3</sub>O<sub>4</sub> crystalline phase. In fact, the topography of such specimens was dominated by close arrays of pyramidal nanoaggregates, resulting in more compact structures with respect to the **A** and **B** cases. The comparison of morphological and structural results suggested that the formation of such peculiar nanoaggregates could be associated with a growth mechanism typical of Co<sub>3</sub>O<sub>4</sub> and, in particular, with the exposure of {111} surface planes, in order to minimize the overall system energy.<sup>31</sup> The mean nanop pyramid size increased from 150 nm, at 400 °C (sample **C**, 400 °C), to 400 nm, at 500 °C (sample **D**).

As already reported,<sup>40</sup> the rms roughness can be used as an estimation of the surface area, whose direct measurement is hard to accomplish by a conventional nitrogen adsorption apparatus on the present nanodeposits because of the low material amount. The rms roughness values for specimens **A–D** obtained from AFM analysis are reported in Table 1. As can be observed, higher rms values were obtained from specimens **A** and **B** deposited at 3.0 mbar total pressure, characterized by the lower particle size and thickness values. In a different way, samples **C** and **D** presented a more compact structure, resulting in a less rough surface topography (compare the pertaining rms values in Table 1) and in a lower active area. These differences will be reflected by diverse electrochemical performances of the obtained specimens, as explained below.

Subsequently, our attention was devoted to the functional investigation of the obtained nanodeposits as electrodes in Li batteries, with particular focus on the interrelations between the system chemicophysical features and the pertaining electrochemical performances. Figure 4 shows galvanostatic discharge–charge curves for the Li/CoO<sub>x</sub> cells in the 3.0–0.0 V range. As

a general trend, the voltage profile shapes were in line with those already described for CoO and Co<sub>3</sub>O<sub>4</sub> electrodes<sup>41,42</sup> and consistent with the occurrence of the following half-reactions:



During the discharge process, both CoO and Co<sub>3</sub>O<sub>4</sub> are reduced, producing nanometric Co particles.<sup>43</sup> It is observed that the nanodeposit Faradic yield exceeds the stoichiometric values for two, five, and eight electrons. This overdischarge phenomenon, frequently observed in similar cases, can be ascribed to the electrolyte reduction, forming a polymeric-like solid electrolyte interphase (SEI) film surrounding the metallic particles and accounting for the potential drop below 0.7 V.<sup>23</sup> The electricity amount involved in the first discharge is only partially extracted in the subsequent charging process. The irreversibility observed for the first discharge/charge process in CoO<sub>x</sub> electrodes was explained in terms of (i) the incomplete decomposition of the Li<sub>2</sub>O during the first charge process<sup>20</sup> and (ii) the incomplete conversion of the Co nanoparticles, obtained after the first discharge cycle, into cobalt oxides.<sup>21,42,43</sup>

As a general trend, the charge curves displayed a similar shape upon cycling for all the analyzed specimens, indicating a high

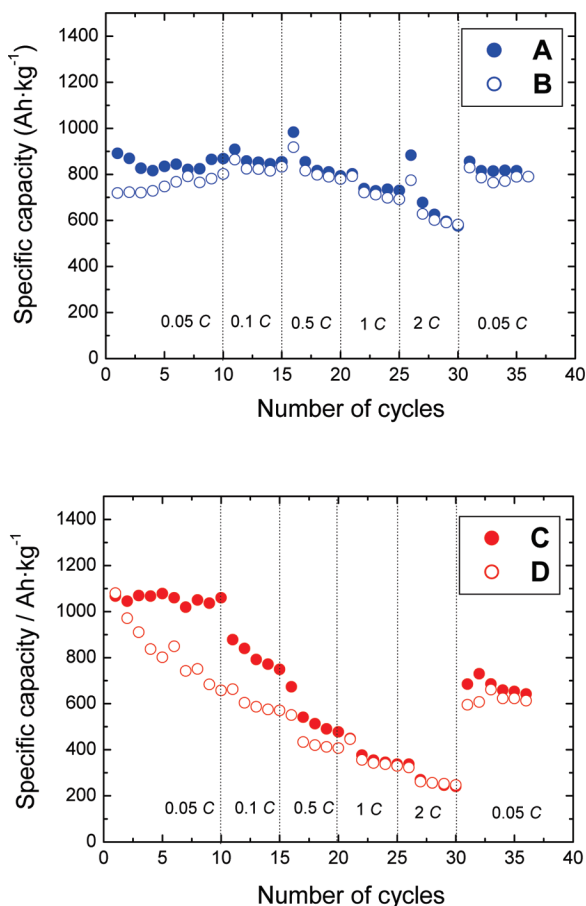


**Figure 5.** Cycling properties of Li/cobalt oxide nanoelectrode cells: delivered specific discharge capacity values vs cycle number for specimens **A–D** cycled at different *C* rates between 3.0 and 0.0 V (vs Li/Li<sup>+</sup>).

reversibility of the electrochemical process, a very attractive feature in view of functional applications of the obtained nanosystems. The observed step potential profiles were typical for the conversion of Co(0) into Co(II) and/or Co(III).<sup>41,42,44</sup> The reversible formation of Li<sub>2</sub>O accompanying the redox processes (eqs 2–4) and the growth of the polymeric layer, resulting from electrolyte degradation, are believed to contribute to the observed Faradic yield.<sup>26</sup>

Figure 5 shows the delivered specific discharge capacity values of the different specimens cycled over the 3.0–0.0 V range at various *C* regimes (see the Experimental Procedures section). The delivered values for samples **A–D** were larger than the expected theoretical ones (715, 850, and 890 mA·h·g<sup>-1</sup>, respectively), indicating the electrochemical participation of electrolyte components upon cycling. The capacity evolution upon fast charging/discharging, from 0.1 to 2 *C*, seemed to be influenced by the pristine particle size of the employed nanoelectrodes. As a matter of fact, specimens **C** and **D**, possessing a higher particle size (mean values = 150 and 400 nm, respectively; see above and Figure 3), exhibited poor capacity retention on cycling, and nearly half of the original values were recovered when the electrodes were charged/discharged again at 0.05 *C* after 30 cycles. In a different way, specimens **A** and **B**, with an average particle diameter lower than 50 nm (see above), possessed good cycling electrochemical performances, with only a 25% loss in the fastest regime, 2*C*.

Notably, for samples **A** and **B**, the delivered capacity was fully recovered after the cycling rate experiments, yielding for both electrodes a mean value of 800 mA·h·g<sup>-1</sup> after 35 cycles.

To the best of our knowledge, this excellent capacity recovery has never been previously reported for electrodes assembled without the use of ancillary materials, like in the present case. These results evidenced the occurrence of the best electrochemical performances in low-sized nanosystems, thanks to the synergistic contribution of the reduced particle dimensions, enabling a faster Li<sup>+</sup> insertion/deinsertion, and the higher active area (compare the rms values in Table 1), promoting a more effective electrode–electrolyte contact.<sup>5,12,14,22,26,27</sup> On the other hand, no correlation was observed between the deposit thickness and their electrochemical behavior, indicating that the electron transfer from the metallic substrate through the whole deposit was not a key factor for the kinetics of the electrochemical reaction.

The specimen phase composition could also have an influence on the observed electrochemical performances. To this regard, whereas some investigators reported on the excellent cyclability of CoO samples,<sup>21,28</sup> other reports have argued on the irreversibility of reaction 4, demonstrating that, during the charge process, the reaction proceeds according to eq 2.<sup>42,43</sup> As a consequence, the full reconversion to Co<sub>3</sub>O<sub>4</sub> would be hindered, resulting in a subsequent capacity loss. This difference in the electrochemical conversion mechanism for CoO and Co<sub>3</sub>O<sub>4</sub> would be favored at high charge/discharge rates, as observed regarding the evolution of capacity values (Figure 5).

To gain a deeper insight into the system electrochemical behavior, a combined FE-SEM and EIS characterization was performed on the discharged electrodes, yielding similar results for specimens **A**, **B** and **C**, **D**, respectively. The impedance spectra obtained in the discharged state at 0.0 V on cycling (the 1st, 10th, and 35th discharge cycle) are presented in Figure 6. For all measurements, the Nyquist plots showed the characteristic depressed semicircle in the high- and middle-frequency range and an extended tail with a slope of ≈45° with respect to the Z' horizontal axis. As previously reported for Co<sub>3</sub>O<sub>4</sub> electrodes,<sup>45,46</sup> only one semicircle was observed, which is considered to arise from the superimposition of two individual contributions at high and medium frequencies. Whereas the former could be attributed to a polymer-like SEI film and/or contact resistance, the latter contribution arose from Li<sup>+</sup> charge-transfer impedance on the electrode/electrolyte interface.<sup>23,45</sup> The inclined linear contribution at ≈45° corresponded to Li-diffusion processes within the obtained systems. In previous reports, the impedance measurements performed in charged/discharged cobalt oxides electrodes showed that the SEI film thickness gradually increases with cycling up to a limiting value.<sup>23,46,47</sup> In this sense, a significant difference was observed for EIS spectra obtained for specimens **A** and **C**. Regarding the former, constituted by 15 nm nanoaggregates, a slight increase of the semicircle took place from the 1st to the 10th discharge cycle. On further cycling, the semicircle became more extended, indicating a progressive growth of the SEI film.

In a different way, concerning specimen **C**, impedance spectra differed both in magnitude and in shape from the 1st to the 10th cycle. After the latter, the observed semicircle shifted toward the intermediate-frequency region, suggesting that the charge-transfer impedance accounted for a large proportion of the overall cell kinetic impedance.<sup>45</sup> The semicircle magnitudes observed for the 1st, 10th, and 35th discharges suggested that a thick SEI film was suddenly formed during the first cycles and becomes stable upon successive cycling.<sup>46</sup> The differences in the formation and stabilization of the SEI film, observed for samples **A** and **C**, could be explained based on their different particle sizes and morphological organization (see above and

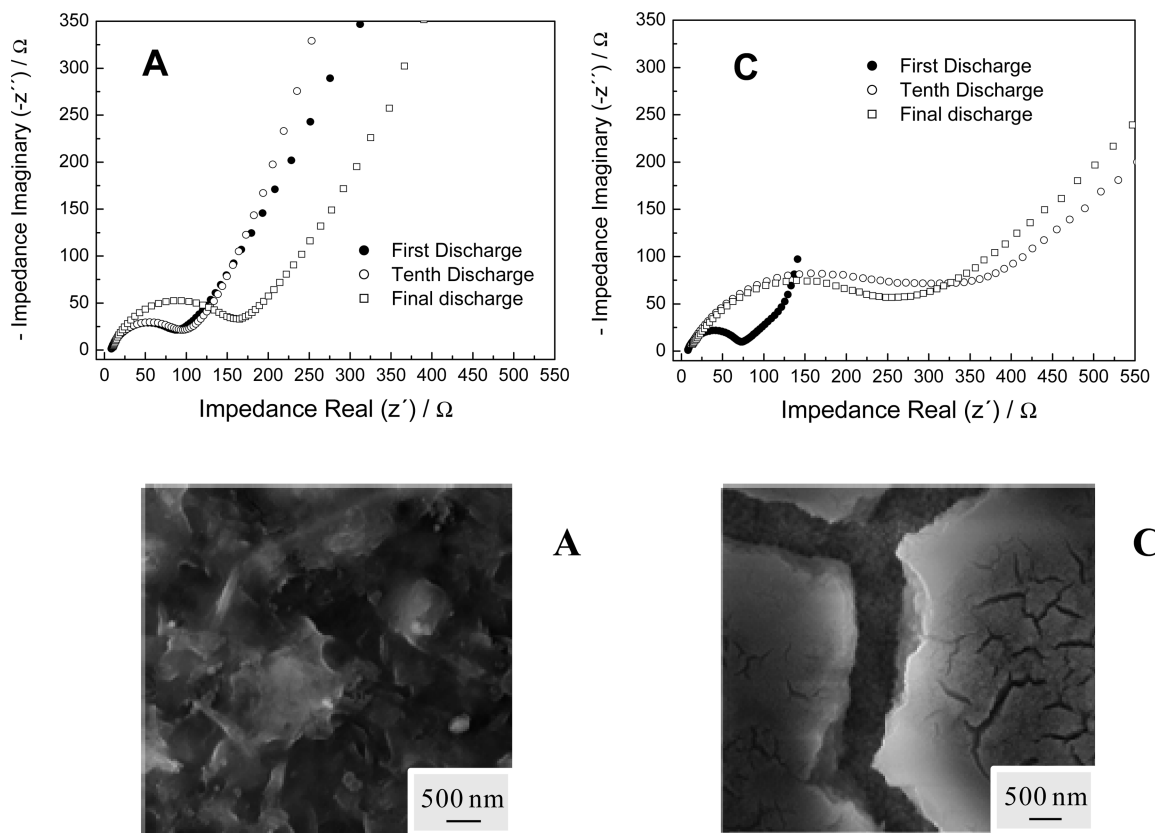


**Figure 6.** EIS spectra for specimens **A** and **C** in the discharged state at 0.0 V (upper). Ex situ FE-SEM images of the electrodes obtained at the end of the cycling tests (lower).

Table 1).<sup>47</sup> The Li<sup>+</sup> charge-transfer impedance values calculated from the different spectra are in agreement with the commented SEI film formation process. To obtain quantitative results, an equivalent circuit with the elements  $R_s$  (solution resistance),  $R_{ct}$  (charge resistance), CPE (constant phase element), and  $W$  (Li<sup>+</sup> diffusion resistance), was used to fit the Nyquist plots.<sup>45</sup>  $R_{ct}$  values of 58.8, 67.6, and 114.6  $\Omega$  for sample **A** and 59.8, 224.3, and 221.3  $\Omega$  for sample **C** were obtained for the 1st, 10th, and 35th discharge, respectively. These results confirm the progressive SEI film formation in sample **A**, whereas for sample **C**, a thicker film is stabilized after the first cycles. As a consequence, on samples **C** and **D**, which are constituted by closely interconnected nanopyramids (150–400 nm in size, resulting in rather flat and compact surface textures; see above), the Li<sup>+</sup> transfer will be obstructed upon cycling. This phenomenon explains the difficulty in maintaining the delivered capacity values when the electrode is charged/discharged at high rates, as observed in Figure 5. As a matter of fact, FE-SEM images recorded after electrochemical tests (Figure 6) provide further support to the proposed explanation. As can be noticed, both electrodes were covered by an SEI film. Whereas in the case of specimen **A** (CoO), a jelly film fully covering the sample surface could be observed, for specimen **C** (Co<sub>3</sub>O<sub>4</sub>), the presence of a thicker coating characterized by extensive cracks was evidenced. The appearance of cracks on the SEI film could be related with the large volume variations experienced by the Co<sub>3</sub>O<sub>4</sub> deposit as a consequence of electrochemical conversion reactions. Such changes introduce mechanical stresses and subsequent microstructural failure that, in turn, prevents an efficient electronic conduction, increasing the charge-transfer resistance.<sup>48</sup> Microstructural deterioration would be favored for compact samples with larger particle dimensions. Consequently, the different morphological features of specimens **A**, **B** in comparison with

**C**, **D** and, in particular, the lower particle size and higher rms roughness values for the former (compare Table 1) could indeed favor the reaction between Li ions and electrons at the electrode interface upon cycling, resulting in an ultimate lower structural deterioration.

### Conclusions

In this work, an innovative procedure for the obtainment of transition-metal oxide nanoelectrodes was proposed. In particular, Co<sub>x</sub>O<sub>y</sub> nanosystems were deposited on Ti substrates by a CVD route starting from a novel molecular precursor, Co(hfa)<sub>2</sub>·TMEDA. A combined selection of the growth temperature and oxygen content in the reaction atmosphere enabled controlling both the phase composition (CoO, Co<sub>3</sub>O<sub>4</sub>, or mixed-phase deposits) and the morphology of the resulting nanosystems. The electrochemical reaction with Li ions was studied in the potential window of 3.0–0.0 V. Remarkably, the obtained results evidenced fast lithium storage for all the investigated specimens. As a matter of fact, high Coulombic efficiencies and high capacity retention upon prolonged cycling were observed for electrodes characterized by smaller-sized particles and a higher surface roughness. The latter systems exhibited a higher interfacial contact area with the electrolyte, enabling thus a shorter Li<sup>+</sup> path length. The excellent capacity recovery was the highest ever obtained up to date for nanoelectrodes assembled without the use of ancillary materials, like in the present case. In a different way, for Co<sub>3</sub>O<sub>4</sub> nanoelectrodes with bigger aggregates and a smoother surface texture, the appearance of extended cracks was indicative of the structural deterioration determined by large volume changes, appreciably hindering charge-transfer processes at high cycling rates.

Overall, the present findings point out the effectiveness and potential of the proposed synthetic strategy for the obtainment

of cobalt oxide nanomaterials as lithium battery negative electrodes. In addition, the reported results highlight the key role of the morphogenesis control in the achievement of improved functional performances for the resulting cobalt oxide nanosystems.

**Acknowledgment.** We thank the Ministerio de Educación y Ciencia (MEC) (Project MAT2008-03160), Junta de Andalucía (Group 175), and University of Córdoba for financial support of this work. PRIN-COFIN 2008, ALADIN Industria 2015 (Ministero dello Sviluppo Economico), CNR-INSTM PROMO, CARIPARO 2006 “Multi-layer optical devices based on inorganic and hybrid materials by innovative synthetic strategies”, and PRAT 2008 “Nano-organization of functional molecular architectures on inorganic surfaces for eco-sustainable processes” programs have provided further financial support. Mr. A. Ravazzolo (CNR, Padova, Italy) is acknowledged for skillful technical assistance. Dr. J. Santos is acknowledged for his helpful assistance in the discussion of the impedance spectra.

## References and Notes

- (1) Armand, M.; Tarascon, J.-M. *Nature* **2008**, *451*, 652.
- (2) Bruce, P. G.; Scrosati, B.; Tarascon, J.-M. *Angew. Chem., Int. Ed.* **2008**, *47*, 2930.
- (3) Li, H.; Wang, Z.; Chen, L.; Huang, X. *Adv. Mater.* **2009**, *21*, 4593.
- (4) Scrosati, B.; Garche, J. *J. Power Sources* **2010**, *195*, 2419.
- (5) Cheng, F.; Tao, Z.; Liang, J.; Chen, J. *Chem. Mater.* **2008**, *20*, 667.
- (6) Kim, M.; Cho, J. *Adv. Funct. Mater.* **2009**, *19*, 1497.
- (7) Wang, Y.; Cao, G. *Adv. Mater.* **2008**, *20*, 2251.
- (8) Poizot, P.; Laruelle, S.; Gruegeon, S.; Dupont, L.; Tarascon, J.-M. *Nature* **2000**, *407*, 496.
- (9) Gómez-Cámer, J. L.; Martín, F.; Morales, J.; Sánchez, L. J. *Electrochim. Soc.* **2008**, *155*, A189.
- (10) Morales, J.; Sánchez, L.; Martín, F.; Berry, F.; Ren, X. *J. Electrochim. Soc.* **2005**, *152*, A1748.
- (11) Morales, J.; Sánchez, L.; Martín, F.; Ramos-Barrado, J. R.; Sánchez, M. *Electrochim. Acta* **2004**, *49*, 4589.
- (12) Lou, X.-W.; Deng, D.; Lee, J.-Y.; Feng, J.; Archer, L. A. *Adv. Mater.* **2008**, *20*, 258.
- (13) Chou, S.-L.; Wang, J.-Z.; Liu, H.-K.; Dou, S.-X. *J. Power Sources* **2008**, *182*, 359.
- (14) Zhan, F.; Geng, B.; Guo, Y. *Chem.-Eur. J.* **2009**, *15*, 6169.
- (15) Wang, Y.; Fu, Z.-W.; Qin, Q.-Z. *Thin Solid Films* **2003**, *441*, 19.
- (16) Gu, Y.; Jiang, F.; Wang, X. *Thin Solid Films* **2008**, *517*, 652.
- (17) Li, W.-Y.; Xu, L.-N.; Chen, J. *Adv. Funct. Mater.* **2005**, *15*, 851.
- (18) Tao, F.; Gao, C.; Wen, Z.; Wang, Q.; Li, J.; Xu, Z. *J. Solid State Chem.* **2009**, *182*, 1055.
- (19) Do, J.-S.; Weng, C.-H. *J. Power Sources* **2005**, *146*, 482.
- (20) Kang, Y.-M.; Kim, K.-T.; Kim, J.-H.; Kim, H.-S.; Lee, P.-S.; Lee, J.-Y.; Liu, H. K.; Dou, S. X. *J. Power Sources* **2004**, *133*, 252.
- (21) Yao, W.; Yang, J.; Wang, J.; Nuli, Y. *J. Electrochim. Soc.* **2008**, *155*, A903.
- (22) Zhang, H.; Wu, J.; Zhai, C.; Ma, X.; Du, N.; Tu, J.; Yang, D. *Nanotechnology* **2008**, *19*, 035711.
- (23) Liu, Y.; Mi, C.; Su, L.; Zhang, X. *Electrochim. Acta* **2008**, *53*, 2507.
- (24) Jiang, J.; Liu, J.; Ding, R.; Ji, X.; Hu, Y.; Li, X.; Hu, A.; Wu, F.; Zhu, Z.; Huang, X. *J. Phys. Chem. C* **2010**, *114*, 929.
- (25) Lu, Y.; Wang, Y.; Zou, Y.; Jiao, Z.; Zhao, B.; He, Y.; Wu, M. *Electrochim. Commun.* **2010**, *12*, 101.
- (26) Nam, K.-T.; Kim, D.-W.; Yoo, P.-J.; Chiang, C.-Y.; Meethong, N.; Hammond, P. T.; Chiang, Y.-M.; Belcher, A. M. *Science* **2006**, *312*, 885.
- (27) Du, N.; Zhang, H.; Chen, B.; Wu, J.; Ma, X.; Liu, Z.; Zhang, Y.; Yang, D.; Huang, X.; Tu, J. *Adv. Mater.* **2007**, *19*, 4505.
- (28) Li, F.; Zou, Q.-Q.; Xia, Y.-Y. *J. Power Sources* **2008**, *177*, 546.
- (29) Fu, Z.-W.; Wang, Y.; Zhang, Y.; Qin, Q.-Z. *Solid State Ionics* **2004**, *170*, 105.
- (30) Li, Y.; Tan, B.; Wu, Y. *Nano Lett.* **2008**, *8*, 265.
- (31) Barreca, D.; Gasparotto, A.; Lebedev, O. I.; Maccato, C.; Pozza, A.; Tondello, E.; Turner, S.; Van Tendeloo, G. *CrystEngComm* **2010**, in press. DOI: 10.1039/b926368n.
- (32) Bandoli, G.; Barreca, D.; Gasparotto, A.; Maccato, C.; Seraglia, R.; Tondello, E.; Devi, A.; Fischer, R. A.; Winter, M. *Inorg. Chem.* **2009**, *48*, 82.
- (33) Gasparotto, A.; Barreca, D.; Devi, A.; Fischer, R. A.; Fois, E.; Gamba, A.; Maccato, C.; Seraglia, R.; Tabacchi, G.; Tondello, E. *ECS Trans.* **2009**, *25*, 549.
- (34) Gruegeon, S.; Laruelle, S.; Dupont, L.; Tarascon, J.-M. *Solid State Sci.* **2003**, *5*, 895.
- (35) Barreca, D.; Gasparotto, A.; Maragno, C.; Tondello, E.; Sada, C. *Chem. Vap. Deposition* **2004**, *10*, 229.
- (36) Barreca, D.; Gasparotto, A.; Maragno, C.; Tondello, E.; Bontempi, E.; Depero, L. E.; Sada, C. *Chem. Vap. Deposition* **2005**, *11*, 426.
- (37) JCPDS Card No. 43-1004, 2000.
- (38) JCPDS Card No. 42-1467, 2000.
- (39) Barreca, D.; Massignan, C.; Daolio, S.; Fabrizio, M.; Piccirillo, C.; Armelao, L.; Tondello, E. *Chem. Mater.* **2001**, *13*, 588.
- (40) Barreca, D.; A. Gasparotto, Maccato, C.; Tondello, E.; Lavrenčič Štangar, U.; Patil, S. R. *Surf. Coat. Technol.* **2009**, *203*, 2041.
- (41) Do, J.-S.; Dai, R.-F. *J. Power Sources* **2009**, *189*, 204.
- (42) Liu, H.-C.; Yen, S.-K. *J. Power Sources* **2007**, *166*, 478.
- (43) Binotto, G.; Larcher, D.; Prakash, A. S.; Herrera Urbina, R.; Hegde, M. S.; Tarascon, J.-M. *Chem. Mater.* **2007**, *19*, 3032.
- (44) Liu, B.; Zhang, X.; Shioyama, H.; Mukai, T.; Sakai, T.; Xu, Q. *J. Power Sources* **2010**, *195*, 857.
- (45) Needham, S. A.; Wang, G. X.; Konstantinov, K.; Lao, Z.; Liu, H. K. *Electrochim. Solid State Lett.* **2006**, *9*, A315.
- (46) Kang, J.-G.; Ko, Y.-D.; Park, J.-G.; Kim, D.-W. *Nanoscale Res. Lett.* **2008**, *3*, 390.
- (47) Liu, Y.; Zhang, X. *Electrochim. Acta* **2009**, *54*, 4180.
- (48) Laruelle, S.; Gruegeon, S.; Poizot, P.; Dolle, M.; Dupont, L.; Tarascon, J. M. *J. Electrochim. Soc.* **2002**, *149*, A627.

JP102380E